

PAPER • OPEN ACCESS

Advanced microwave method for electron density profile reconstruction of an atmospheric plasma torch

To cite this article: Christos Vagkidis *et al* 2025 *Plasma Sources Sci. Technol.* **34** 105004

View the [article online](#) for updates and enhancements.

You may also like

- [Simulation study of mode transitions induced by external control parameters in capacitively coupled oxygen discharges](#)
Chong-Biao Tian, Li Wang, Máté Vass *et al.*
- [Electrical charge decay on dielectric surface in nitrogen/C₂F₄/N mixtures](#)
D Prokop, M Mrkviková, J Tungli *et al.*
- [Self-consistent global plasma model with application to a microwave electrothermal thruster with atomic propellants](#)
M Lauriola, M Nava, A Maffini *et al.*

Advanced microwave method for electron density profile reconstruction of an atmospheric plasma torch

Christos Vagkidis^{1,*} , Andreas Schulz¹ , Stefan Merli¹ , Mirko Ramisch¹ , Eberhard Holzhauser¹, Walter Kasperek¹ , Günter E M Tovar^{1,2}  and Alf Köhn-Seemann^{1,*} 

¹ Institute for Interfacial Process Engineering and Plasma Technology IGVP, University of Stuttgart, Pfaffenwaldring 31, 70569 Stuttgart, Germany

² Fraunhofer Institute for Interfacial Engineering and Biotechnology IGB, Nobelstr. 12, 70569 Stuttgart, Germany

E-mail: christos.vagkidis@igvp.uni-stuttgart.de and koehn@igvp.uni-stuttgart.de

Received 19 March 2025, revised 18 August 2025

Accepted for publication 16 September 2025

Published 6 October 2025



Abstract

Microwave interferometry is a reliable, well established, and non-perturbing method to measure the line-integrated electron density of a non-uniform plasma through the phase shift of a wave that propagates the plasma medium. In this paper we combine the phase shift and the attenuation of the wave to experimentally extract both, the line-integrated density and the electron–neutral collision frequency of an atmospheric plasma torch. In addition, a novel method to obtain the 2D spatial plasma density profile of the torch is demonstrated by measuring the microwave power, without any information of the phase. The receiving antenna of the interferometer is moved perpendicularly to the axis of the torch and measures the spatial distribution of the microwave power. The wave is scattered by the plasma and the scattering profile depends on the plasma density profile. Direct comparison of this scattering profile with 3D full-wave simulations provides information on the electron number density profile of the plasma torch.

Keywords: atmospheric plasma torch, line-integrated density, collision frequency, plasma density, microwave interferometry, COMSOL Multiphysics, 3D full-wave simulations

1. Introduction

Microwave atmospheric plasma torches are widely used in industrial applications [1]. They can be used, among others, for fabrication of diamond nanopowder [2], carbon dioxide (CO₂) conversion to carbon monoxide (CO) and oxygen (O₂) [3–6], nitrogen oxides formation [7, 8], and coal gasification

[9]. In order to fully understand and further optimize these processes, it is important to precisely evaluate the fundamental plasma parameters. Among these parameters, the electron density and the electron–neutral collision frequency are of high importance.

There are two major diagnostic categories used for experimentally obtaining the plasma density: passive and active plasma diagnostics [10]. The former is using radiation from the plasma itself, while the latter is measuring changes in external beams that are used to probe the plasma. Microwave diagnostics, such as interferometry or reflectometry are typical active diagnostics used in plasma applications [11, 12].

Langmuir probes are one of the most common passive approaches to obtain profiles of both, the plasma density and the electron temperature [13–16]. They have the advantage of

* Authors to whom any correspondence should be addressed.



Original Content from this work may be used under the terms of the [Creative Commons Attribution 4.0 licence](https://creativecommons.org/licenses/by/4.0/). Any further distribution of this work must maintain attribution to the author(s) and the title of the work, journal citation and DOI.

providing accurate measurements with high spatial resolution. However, they cannot directly measure the collision frequency in the plasma. Moreover, in the case of a microwave plasma at atmospheric pressure, the neutral gas temperature is high enough to melt a typical probe [17].

Single-chord microwave interferometry on the other hand, even though it has no spatial resolution along the beam, can simultaneously diagnose the line-integrated density and the collision frequency of the plasma [18]. Good agreement of plasma density measurements performed with Langmuir probes and microwave interferometry has been shown in [19] and [20].

Microwave interferometry utilizes the interference between two waves; the first beam is propagating in free space, while the second one is used to probe the plasma and experiences a phase shift. The phase difference between the two beams in turn can be used to yield either the absolute density of a homogeneous plasma or the line-integrated density of an inhomogeneous plasma [21].

The collision frequency is obtained by measuring in addition the attenuation of the wave that crosses the plasma. The two measured quantities, phase shift and attenuation, are related to the refractive index of the plasma by the Appleton–Hartree equation [22]. This enables the numerical calculation of both, the line-integrated density and the collision frequency, without needing information on the electron temperature or the electron–neutral collision cross-section.

In this paper, microwave interferometry is applied to obtain the line-integrated density and the electron–neutral collision frequency of an atmospheric plasma torch based on experimental results. Additionally, a 2D spatially resolved electron density profile of the torch is estimated by measuring the spatial power profile of a wave after propagating across the torch and comparing this result against 3D full-wave simulations, which are performed with the COMSOL Multiphysics software.

2. Theoretical background

Assuming an isotropic, unmagnetized plasma, the real and imaginary parts of the complex refractive index for an electromagnetic wave, $\tilde{\mu} = \mu - j\chi$, can be expressed as [23]

$$\mu = \left\{ \frac{1}{2} \left(1 - \frac{\omega_{pe}^2}{\omega^2 + \nu_{en}^2} \right) + \frac{1}{2} \left[\left(1 - \frac{\omega_{pe}^2}{\omega^2 + \nu_{en}^2} \right)^2 + \frac{\nu_{en}^2}{\omega^2} \left(\frac{\omega_{pe}^2}{\omega^2 + \nu_{en}^2} \right)^2 \right]^{1/2} \right\}^{1/2} \quad (1)$$

and

$$\chi = \left\{ -\frac{1}{2} \left(1 - \frac{\omega_{pe}^2}{\omega^2 + \nu_{en}^2} \right) + \frac{1}{2} \left[\left(1 - \frac{\omega_{pe}^2}{\omega^2 + \nu_{en}^2} \right)^2 + \frac{\nu_{en}^2}{\omega^2} \left(\frac{\omega_{pe}^2}{\omega^2 + \nu_{en}^2} \right)^2 \right]^{1/2} \right\} \quad (2)$$

where ω_{pe} is the electron plasma frequency, ω the microwave frequency, and ν_{en} the electron–neutral collision frequency. Equation (2) demonstrates the physical relation between plasma collisionality and attenuation. If $\nu_{en} \rightarrow 0$ then the attenuation index, χ , goes to zero as well. The spatio-temporal evolution of the wave electric field can be written as [24]

$$E(z, t) = E_0 \exp \left[j \left(\omega t - \tilde{k}z \right) \right], \quad (3)$$

where \tilde{k} is the complex propagation constant, $\tilde{k} = \beta + j\alpha$, with β and α the phase and attenuation coefficients, respectively. The phase coefficient, β , is related to the real part of the refractive index, μ , through the relation

$$\beta = \mu \frac{\omega}{c}, \quad (4)$$

while the attenuation coefficient, α , is linked to the attenuation index, χ , as

$$\alpha = \chi \frac{\omega}{c}, \quad (5)$$

with c the speed of light in vacuum. From equations (3) and (5), the attenuation in dB of a plane electromagnetic wave through the plasma can be obtained as [25]

$$\alpha = 10 \log_{10} \left[\left(\frac{E}{E_0} \right)^2 \right] = 10 \log_{10} \left[\exp \left(\frac{-2d\omega}{c} \chi \right) \right], \quad (6)$$

where d is the length of the plasma. The wave is suffering a phase change due to the plasma, $\phi_p = (\omega/c)\mu d$. When compared to the phase in free space, $\phi_0 = (2\pi/\lambda_0)d$, the phase difference is

$$\Delta\phi = \phi_p - \phi_0 = \left(\frac{\omega}{c}\mu - \frac{2\pi}{\lambda_0} \right) d, \quad (7)$$

with λ_0 the wavelength in free space.

Equations (6) and (7) are linking the attenuation and the phase difference of the wave to the probing frequency, ω , the plasma length, d , and the components of the complex refractive index. The μ and χ are functions of the plasma frequency, ω_{pe} , and the electron–neutral collision frequency, ν_{en} , while ω and d are fixed for a specific experimental apparatus. Since the electron density n_e is included in the plasma frequency as $\omega_{pe} = \sqrt{n_e e^2 / (m_e \epsilon_0)}$, equations (6) and (7) are essentially becoming functions of n_e and ν_{en} . Thus, if the attenuation and the phase difference of a wave that is traveling through the plasma are known, the electron density and the collision frequency can be numerically calculated.

3. Experimental set-up

3.1. The atmospheric plasma torch

A schematic representation of the microwave-generated plasma torch used in this work [26–28] is given in figure 1.

The microwaves of frequency 2.45 GHz are generated by the magnetron (model MH3000S-211BA manufactured by

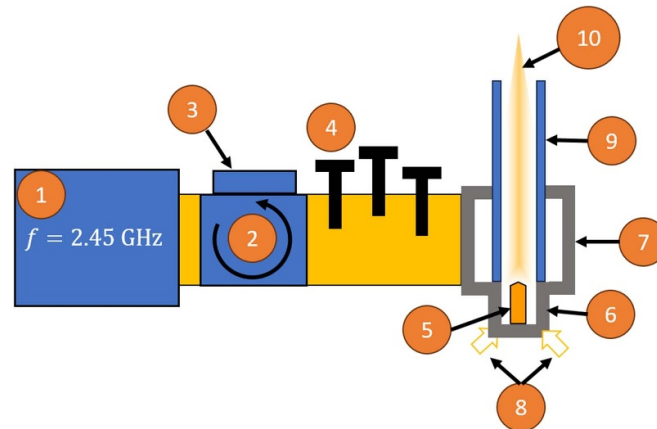


Figure 1. Schematic representation of the plasma torch with the components numbered: (1) magnetron; (2) circulator with (3) water load; (4) three-stub tuner; (5) ignition tip; (6) coaxial resonator; (7) cylindrical resonator; (8) tangential gas inlets; (9) quartz glass tube; (10) plasma flame.

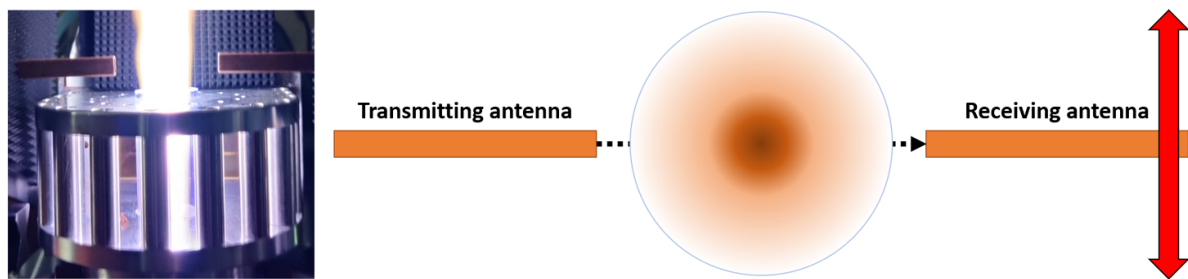


Figure 2. (Left) Picture of the plasma torch in operation and (right) top view of the network analyzer's antennas mounted on the torch. The measurements are performed at the outlet of the plasma torch, above the end of the cylindrical resonator.

Muegge) and are fed into the plasma via a rectangular waveguide. The magnetron provides a nominal heating power up to 3 kW. The circulator, which is connected to a water load, protects the magnetron from reflected power from the recipient. The auto three-stub tuner is used to match the impedances and thus, is ensuring maximum forward microwave power and minimum reflected power. The HomTool software (version 5.0.0.4) by S-TEAM is used to measure the incoming and the reflected power, providing the exact power that is deposited into the plasma.

A combination of four tangential gas inlets (only two are shown in figure 1) provides the gas into the coaxial resonator and ensures plasma stability by a strong upward rotating flow [29]. In this particular configuration gas flows up to 100 standard liter per minute (slm) can be achieved. The microwaves are coupled into the coaxial resonator, creating a maximum electric field at the top of the ignition tip where the plasma is ignited. After the ignition, the plasma moves to the cylindrical resonator where it can operate in steady state. A quartz glass tube, with inner and outer diameter of 26 mm and 30 mm respectively, is used to confine the plasma. The gas used for the experiments is dry, compressed air and the gas flow is set at 14 slm.

3.2. The microwave diagnostics

As explained in section 2, in order to obtain simultaneously the line-integrated density and the collision frequency of the plasma torch, both the phase shift and the wave attenuation are needed. A vector network analyzer (MVNA-8-350 manufactured by AB Millimetre) is a suitable measuring system for this task, as it can provide both quantities simultaneously. The measurements are performed at the outlet of the plasma torch, just above the end of the resonator and the quartz glass tube. The antennas of the network analyzer mounted on the plasma torch in operation are shown in figure 2.

A probing microwave frequency of $f_0 = 140$ GHz is chosen to ensure that cut-off effects do not play a role. The microwave is emitted from the transmitting antenna (left), it crosses the plasma perpendicularly with respect to the torch axis and is detected by the receiving antenna (right). For both antennas, rectangular WR28 waveguides are used with cross-section of 7.112 mm and 3.556 mm. As it can be seen in figure 2 (left), absorbing materials are installed around the antennas to reduce beam reflections. The reference wave is provided by the network analyzer and thus a reference beam is not needed. The network analyzer is measuring both, the phase difference and the wave attenuation caused by the plasma.

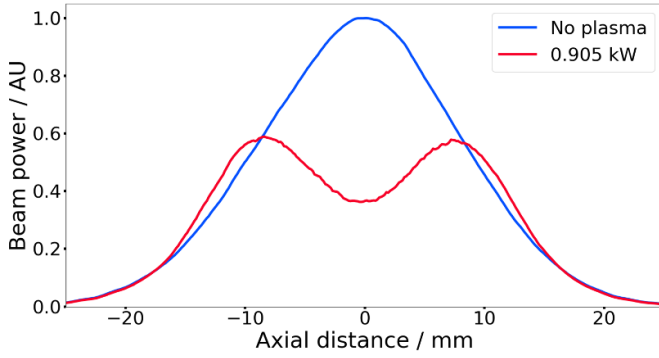


Figure 3. Typical beam power profiles. The gas flow is set at 14 slm for both cases and the heating power at 0.905 kW for the example including plasma.

Even though the line-integrated density and the collision frequency can be extracted with this set-up, it is not possible to obtain information on the electron density profile. This can be achieved by measuring the spatial profile of the output power of the wave that crosses the plasma.

In order to measure the power profile, the receiving antenna of the network analyzer is mounted on a stepping motor, which operates with submillimeter precision. It is then moved in one dimension, perpendicularly to the plasma torch, as illustrated by the red arrow in figure 2 (right). A typical beam power profile of a wave that has crossed the plasma, as well as a power profile in the absence of the plasma for reference, is shown in figure 3.

The microwave beam is clearly perturbed by the presence of the plasma, as it appears to be scattered. The shape of the scattering profile depends on the electron density profile as will be shown in section 6.

4. COMSOL Multiphysics software

The line-integrated density and the collision frequency of the plasma torch can be obtained from experimental data and they are presented in section 5. However, in order to obtain the 2D density profile, additional full-wave simulations are required. Simulations are carried out with the COMSOL Multiphysics software, utilizing the Radio-Frequency (RF) module [30].

COMSOL uses the Finite Element Method (FEM) to approximately solve the wave equation,

$$\nabla \times \mu_r^{-1} (\nabla \times \mathbf{E}) - k_0^2 \left(\epsilon_r - \frac{j\sigma}{\omega\epsilon_0} \right) \mathbf{E} = 0, \quad (8)$$

where μ_r is the relative permeability, \mathbf{E} the electric field vector, ϵ_r the relative permittivity, σ the electrical conductivity, ω the probing angular frequency and ϵ_0 the permittivity in free space. The plasma profile is defined through the ϵ_r and will be explained in detail in section 4.2. In order to accurately simulate the plasma torch, a custom 3D model has been developed for this work. Several research papers utilizing the electromagnetic modules of COMSOL have been published

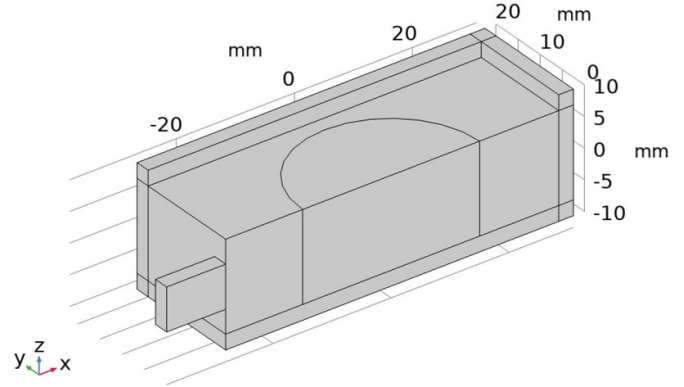


Figure 4. The geometry of the 3D COMSOL model. The transmitting antenna (left side), an air chamber and the plasma (half circle in the center of the domain) are included in the model. The boundaries are set to PML, while the xz -plane at $y = 0$ is a symmetry plane.

[31–35]. Nevertheless, a benchmark of the particular model used in this report was carried out. If the reader is interested in the validation of the model, please refer to the [appendix](#).

4.1. The geometry of the model

The first step is to create the geometry of the model. A picture of the geometry is shown in figure 4.

As mentioned in section 3.1, the four tangential gas inlets provide a stable and horizontally symmetric plasma. This means that the system can be considered as mirror symmetric, ergo only half the geometry needs to be included, as presented in figure 4. This is a crucial step for the model development as it effectively halves the overall number of elements, saving thus significant computational time and memory. The mirror symmetry of the problem can also be justified from the two almost identical peaks of the experimental result, which is the red curve in figure 3.

As can be seen in figure 4, the transmitting antenna, an air chamber and the plasma column are simulated. The surrounding layers are the boundaries of the system, which are set to perfectly matched layers (PMLs). The PMLs ensure that the fields are absorbed at the boundaries of the model and no reflected fields are returning into the domain of interest. The xz -plane at $y = 0$ is a symmetry plane, which allows the mirroring of the solution once the simulation is completed. The top PML in figure 4 is intentionally hidden, in order to allow the plasma column to be visible.

The next step is to define a suitable mesh for the model. As demonstrated in [31], when using the RF module of COMSOL with a grid consisting of five elements per wavelength the errors are less than 5%. With a probing frequency of $f_0 = 140$ GHz, the corresponding (vacuum) wavelength is $\lambda_0 \approx 2.141$ mm. An adaptive mesh is selected in COMSOL, which scales between $\lambda_0/4$ and $\lambda_0/6$, ensuring extra fine meshing in the areas of interest, and less fine meshing for the far-field calculations. A typical mesh of this model consists of approximately 1.95×10^6 elements.

A full 3D simulation with parallel computing on Intel(R) Xeon(R) CPU E5-2690 v2 @ 3.00 GHz (using 20 threads) requires roughly 2 h to be completed. The system that is used for the calculations has a maximum of 128 GB RAM, while the model is using approximately 50% of those.

4.2. The plasma profile

The Drude model is used to simulate the plasma profile as a material in COMSOL. The relative permittivity is adjusted in order to include the plasma profile. According to the Drude model, the relative permittivity of the plasma is [36]

$$\epsilon_r = 1 - \frac{\omega_{pe}^2}{\omega(\omega - j\nu_{en})}. \quad (9)$$

The remaining geometry is filled with air with $\epsilon_r = 1$. The electron density, n_e , is included in the plasma frequency ω_{pe} . Equation (9) includes damping effects through the electron-neutral collision frequency term, ν_{en} . A 2D higher-order Gaussian profile has been selected for the electron density, as it is a generic profile and can capture the profile of the plasma torch:

$$n_e(x, y) = A \exp\left(-\left(\frac{(x-x_0)^2}{2\sigma_x^2} + \frac{(y-y_0)^2}{2\sigma_y^2}\right)^\beta\right), \quad (10)$$

with $A = \frac{n_e}{n_c}$ the peak density, normalized to the cut-off density $n_c = \omega^2 \epsilon_0 m_e / e^2 \approx 2.1 \times 10^{20} \text{ m}^{-3}$ for the probing frequency $f_0 = 140 \text{ GHz}$. As can be seen in equation (10), there is no variation along the z -direction, which means that the plasma is assumed to be homogeneous along the vertical direction (direction z in figure 4). It should be noted that this assumption holds for the area of interest, which is the first 10 to 15 mm above the resonator, where the measurements are performed [37].

The plasma profile is therefore controlled by three parameters included in equation (10):

- A : the peak electron number density, normalized to the cut-off density for the probing frequency $f_0 = 140 \text{ GHz}$.
- $\sigma_x = \sigma_y = \sigma$: the standard deviation that controls the width of the Gaussian ‘bell’.
- β : the exponent, which controls the shape of the distribution.

Figure 5 shows an example of the wave electric field of a 3D simulation. The beam scattering can be seen in the direction of propagation (x), as well as on the yz -plane. In this example, the peak density has been set to a value that is close to the cut-off density for illustration purposes ($A = n_e/n_c = 0.9$).

5. Line-integrated density and collision-frequency

The line-integrated density and the collision frequency of the plasma torch can be obtained through equations (6) and (7), as explained in section 2. A typical measurement from the network analyzer is presented in figure 6. Generally, the experiments are performed as follows:

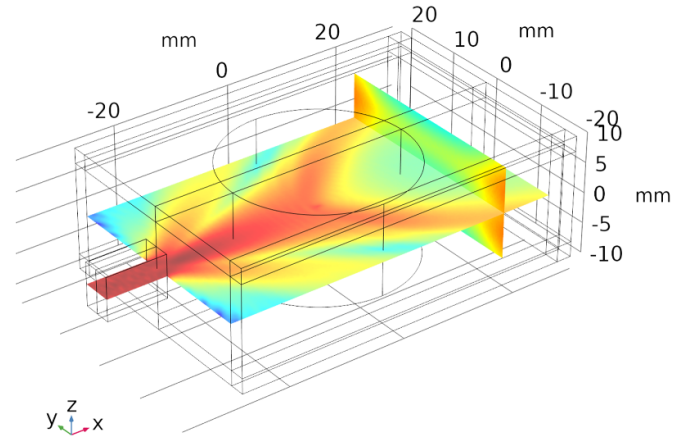


Figure 5. The wave electric field of a 3D COMSOL simulation. The wave can be clearly seen scattered by the plasma. The peak density of the plasma is set to a high value ($A = n_e/n_c = 0.9$) for illustration purposes.

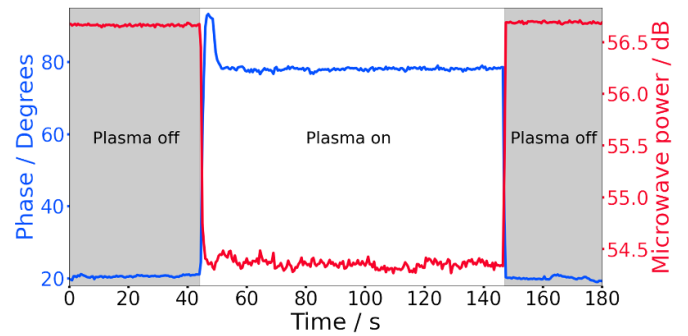


Figure 6. Typical measurement of the network analyzer. The phase difference caused by the plasma is plotted in blue and the microwave beam power in red.

- Step 1: The measurement with the network analyzer is started without the presence of the plasma, which corresponds roughly to the first 45 s of figure 6.
- Step 2: The plasma is ignited, as it can be seen in figure 6 around $t = 50 \text{ s}$ where both the phase and the microwave power are abruptly changing.
- Step 3: The plasma is turned off and both phase and microwave power are returning to their initial values.

The quantities are then averaged in each stage and the attenuation, α , and the phase difference, $\Delta\phi$, are calculated to be used in equations (6) and (7) respectively. This process is repeated for several values of heating power from the magnetron, in order to investigate how the density and the collision frequency are scaling with respect to the heating power. The results are plotted in figure 7.

Figure 7 (left) contains the line-integrated and the peak density of the plasma torch. For these calculations, the plasma profile is approximated as a Gaussian function. As expected, the electron density is increasing with increasing heating power from the magnetron, corresponding to the increased

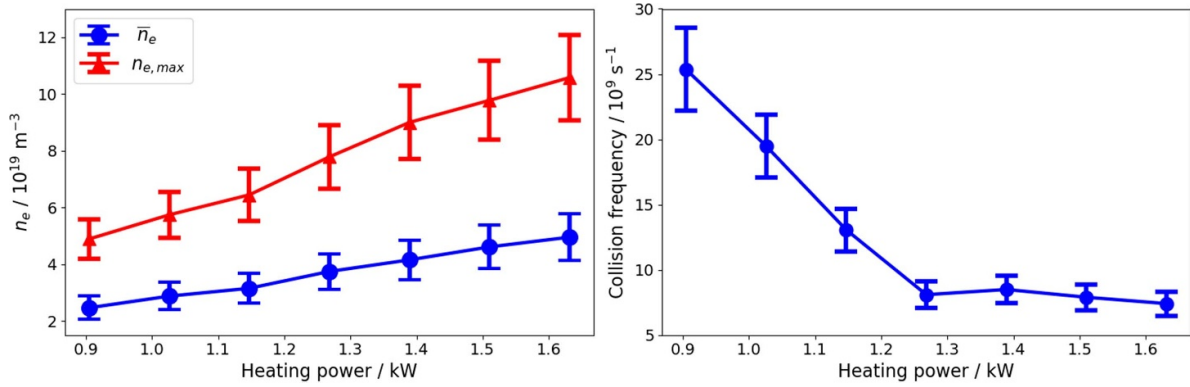


Figure 7. (Left) Line-integrated and maximum density and (right) electron–neutral collision frequency of the plasma torch as a function of the heating power. Note that zero has been suppressed in both figures.

degree of ionization. Qualitatively, this behavior of the electron density was also observed in [26], where a calculation of the electron density through Saha’s equation was carried out.

As shown in figure 7 (left), the line-integrated density scales linearly with heating power between $\bar{n}_e = 2.46 \times 10^{19} \text{ m}^{-3}$ and $\bar{n}_e = 4.95 \times 10^{19} \text{ m}^{-3}$, while the peak density scales between $n_{e,max} = 4.88 \times 10^{19} \text{ m}^{-3}$ and $n_{e,max} = 1.05 \times 10^{20} \text{ m}^{-3}$. It is worth noting that these values of electron density are well above the cut-off density for the microwaves used for igniting and heating the plasma, which is $n_c \approx 7.4 \times 10^{16} \text{ m}^{-3}$ for $f = 2.45 \text{ GHz}$.

However, collisions allow the microwave to penetrate and effectively heat the plasma, which makes the collision frequency a key parameter. The characteristic length over which the electromagnetic wave penetrates into the plasma and deposits energy is known as the skin depth. As described in [38], electron–neutral collisions significantly influence the skin depth by modifying the plasma’s effective conductivity and dielectric response, thereby impacting the field penetration and heating profile.

The electron–neutral collision frequency is plotted in figure 7 (right). In contrast to the electron density, the collision frequency is decreasing with increasing heating power up to $\sim 1.3 \text{ kW}$ and then it stays constant. The electron–neutral collision frequency is given by [39]

$$\nu_{en} = n_a \langle \sigma_{ea} v_{th} \rangle, \quad (11)$$

where n_a is the neutral particle density, v_{th} the thermal velocity of the electrons (the neutral thermal velocity can be neglected as it is significantly lower than the electron velocity), and σ_{ea} the electron–neutral collision cross section. As mentioned in section 3.1, the gas used in the experiments is dry, compressed air, which consists of $\sim 78\%$ nitrogen. Therefore, the electron–nitrogen molecule cross section is used.

The 2.45 GHz microwave is heating the light electrons, resulting only in a slight increase of the electron temperature, between 0.46 eV and 0.49 eV when the heating power is varied between 0.73 kW and 2.35 kW [26]. For this energy range the electron–nitrogen cross section, σ_{ea} , of equation (11) can be considered constant [40].

The neutral particles in the plasma are heated through collisions with the lighter electrons. The slightly increasing electron temperature leads to moderately increased electron thermal velocity ($v_{th,e} \propto T_e^{1/2}$). Consequently, the neutral particle temperature is slightly increased as well.

Higher neutral temperature results, however, in lower neutral particle density, according to Dalton’s law:

$$n_a = \frac{p}{k_b T_a}, \quad (12)$$

assuming that $n_a \gg n_i = n_e$ ($n_a \approx 2 \times 10^{24} \text{ m}^{-3} \gg n_e \approx 10^{20} \text{ m}^{-3}$ inside the resonator [26]) so that the ion and electron densities can be neglected and the gas pressure is constant and equal to the surrounding atmospheric pressure. This is in agreement with figure 7 (left), which demonstrates the increasing electron density and indicates the increased degree of ionization.

According to equation (11), the collision frequency scales as $\nu_{en} \propto n_a$ and $\nu_{en} \propto \sqrt{T_e}$, so the neutral particle density is believed to be the driving term for the decreasing branch of figure 7 (right), between $\sim 0.9 \text{ kW}$ and $\sim 1.25 \text{ kW}$.

The collision frequency, however, stays constant for higher heating power. This is probably due to the fact that the collision frequency is strongly related to the heating efficiency of the plasma. The absorbed power, P_A , by the electrons per unit volume can be expressed as [41]

$$\frac{P_A}{E^2} = \frac{n_e}{n_c} \epsilon_0 \omega \frac{\nu_{en}/\omega}{1 + (\nu_{en}/\omega)^2}, \quad (13)$$

where E is the electric field intensity. Figure 8 plots the absorbed power as a function of the ratio ν_{en}/ω for different electron density values n_e/n_c .

It can be seen that the absorbed power is always peaking in the $\nu_{en}/\omega = 1$ region, regardless of the density. Higher heating power means that more power is deposited into the plasma. As the power is increasing, the collision frequency is decreasing, until it reaches the optimum value of $\nu_{en}/\omega \approx 1$. As the collision frequency remains constant at $\nu_{en} \approx 7 \text{ GHz}$ and the microwave frequency is 2.45 GHz, the ratio is approximately $\nu_{en}/\omega \approx 3$, which is close to the optimum value of

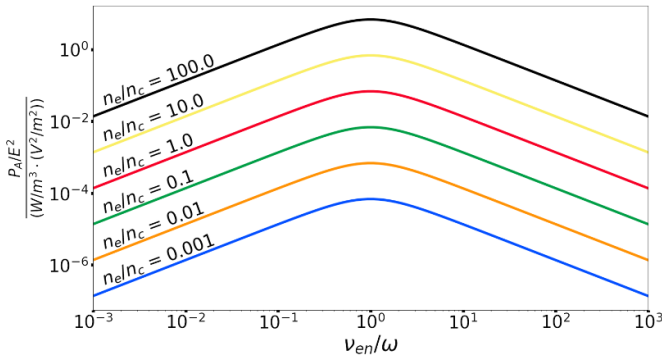


Figure 8. Power absorption as a function of the ν_{en}/ω for different ratios of n_e/n_c . The absorbed power has a maximum at $\nu_{en}/\omega = 1$ for every density ratio.

1 and provides a possible explanation of the observed trend in figure 7 (right) for heating power between ~ 1.3 kW and ~ 1.65 kW.

The higher than the optimum $\nu_{en}/\omega = 1$ observation can be attributed to mainly two reasons. Firstly, inelastic collisions play a significant role in the energy transfer process, thus leading to an enhanced collision frequency needed to achieve the best absorption.

Moreover, the calculations presented in figure 7 (right) represent the collision frequency as a line-averaged quantity. Since the electron density is not uniform, the collision frequency is also not uniform. The major power deposition takes place near the plasma edge, where the collision frequency is expected to be lower than the center and most probably closer to the ideal $\nu_{en}/\omega = 1$.

6. 2D plasma density profile

In section 3.2 the moving receiving antenna was introduced and a typical example of a beam scattering profile was plotted in figure 3. Similarly to the line-integrated density and the collision frequency measurements, the profile of the plasma torch is investigated with respect to the heating power from the magnetron. The first step is to measure the spatial distribution of the wave power for different heating powers. The step size of the radial scan is 0.15 mm. The results are plotted in figure 9. All curves are normalized to the reference case, which is the one that does not include the plasma.

A clear trend is observed in figure 9. Higher heating power leads to lower total detected power measured from the receiving antenna of the network analyzer. Statistical errors are estimated to be less than 1% in each case and hence error bars are not included in figure 9³.

As demonstrated by the red arrow in figure 2 (right), the receiving antenna is moving in one dimension, perpendicularly to the torch axis. In addition to the scattering, which is clearly visible in figure 9, the beam experiences a broadening along the vertical direction (along the plasma column),

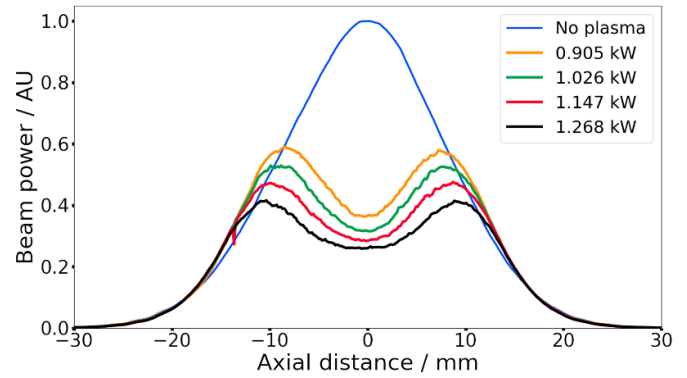


Figure 9. Scattered beam power profiles for different heating powers. The power profile in the absence of the plasma (blue) is plotted as well for reference.

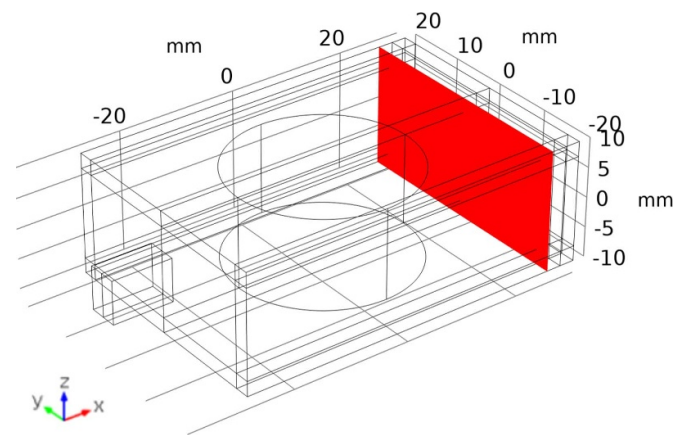


Figure 10. yz -plane of the 3D COMSOL model. The wave power is monitored across the whole yz -plane. The illustrated yz -plane is located exactly at the receiving antenna x -position.

which is not captured by the receiving antenna due to the aforementioned one-dimensional movement. This broadening can be confirmed from the 3D simulations by monitoring the wave power across the whole yz -plane, which is indicated in figure 10.

The model is run twice, once without the plasma and once with the plasma, respectively. The surface integral of the wave power of the yz -plane is then calculated for each case. A typical plasma profile was used for this simulation with the following parameters: $n_e/n_c = 0.3$, $\sigma_x = \sigma_y = 2.5$, $\beta = 0.25$. The surface integrals can be calculated directly in COMSOL and are presented here in arbitrary units (AU):

- Without plasma = 9.3611 AU.
- With plasma = 9.1180 AU.

It is shown that the surface integral is reduced only by 2.5%, which demonstrates that almost the whole microwave power is deposited in the yz -plane. The 2.5% drop could be explained as outgoing power towards the PMLs of the model. As the wave frequency, $f_0 = 140$ GHz, is well above the plasma frequency, microwave power is not expected to be deposited in the plasma.

³ The statistical errors are estimated as the element-wise mean value of the residuals between three consecutive measurements.

However, a line integration of the same case results in 20% drop of microwave power. The line integration is performed along the $z = 0$ of the yz -plane, which corresponds to the center of the receiving antenna in the experimental apparatus. The difference between the surface and line integration of the microwave power provides an explanation for the observed trend in figure 9.

The next step is to perform an extensive variation of the density profile parameters of equation (10) and then compare the simulation results against the beam scattering profiles of figure 9. In order to achieve experimental relevance, the following range is selected:

- $n_e/n_c = 0.2 - 0.5$
- $\sigma_x = \sigma_y = 2 - 7.5$
- $\beta = 0.1 - 0.6$.

The 1D beam scattering profile is calculated in the simulation domain and each of these simulation results is interpolated and compared against all of the experimental results. The coefficient of determination, R^2 , is chosen for the comparison:

$$R^2 = 1 - \frac{\sum_{i=1}^n (Y_i - \tilde{Y}_i)^2}{\sum_{i=1}^n (Y_i - \bar{Y})^2}, \quad (14)$$

where Y_i represents the experimental result, \tilde{Y}_i the simulation result and \bar{Y} the mean value of the experimental result. The simulation result that returns the closest to $R^2 = 1$ is selected as the closest to the real profile and then the plasma parameters are slightly adjusted in order to increase the R^2 score further.

Figure 11 summarizes the results of this comparison. On the left side of the figure, the beam scattering profiles are plotted. Each plot corresponds to a different heating power from the magnetron, starting from 0.905 kW and up to 1.268 kW. The beam profile in the absence of the plasma is plotted in every subfigure for reference. The residuals, $Y_i - \tilde{Y}_i$, are plotted below each beam scattering profile comparison (only for the results including plasma). On the right side of each subfigure, the plasma density profile used in the simulation causing the corresponding scattering profile is displayed. The blue filled circles of the plasma profiles' curves reflect COMSOL's grid.

A very good agreement is observed for the first three cases, which correspond to 0.905 kW, 1.026 kW, and 1.147 kW. The simulation results are following closely the experimental ones, as can be seen from the beam scattering profiles and the residuals, which are almost zero across the whole axis. The achieved R^2 scores are 0.974, 0.962, and 0.950, respectively. For the last case, 1.268 kW, the simulation result is following the experimental result very well in shape, but it is slightly higher in absolute value across the axis. The R^2 score for this case is 0.875.

Similarly to figure 7 (left), the peak electron density is increasing for increased heating power in figure 11. However, additional information is obtained from the latter graph. The width of the plasma, which is linked to the parameter σ , is

increasing as well with respect to the heating power. The shape of the distribution, controlled by the parameter β , is similar in all cases as it peaks in the central region and is decreasing towards the edges. Table 1 contains the exact parameters of equation (10) that were used in the 3D simulations and returned the highest R^2 scores when compared against the experimental results. The achieved R^2 score for each case is also included in table 1.

A steep change in parameters σ and β is observed when going from 1.026 kW to 1.147 kW. These two parameters are correlated, since they are both controlling the spreading of the electron density distribution. While σ is increasing, β is decreasing. This antiparallel change leads to a very similar spreading, as it can be observed in the plasma profiles plotted in figure 11 (right, second and third profiles).

The centrally peaked plasma profile above the cylindrical resonator is in good agreement with the results from [26], where a spatially resolved electron density profile was obtained through Saha's equation.

7. Conclusions

Electron density and collision frequency measurements of an atmospheric plasma torch were performed with microwave diagnostics. By using a network analyzer for interferometry measurements, the line-integrated density and the electron-neutral collision frequency were numerically calculated from the measured wave attenuation and phase difference. The line-integrated and the maximum density were found to constantly increase for increased heating power, which is explained from the increased degree of ionization. On the other hand, the collision frequency was observed to decrease at first, until it reached a constant value, which corresponds to $\nu_{en}/\omega \approx 3$, with ω the angular frequency of the magnetron. This value is close to the optimum value of $\nu_{en}/\omega \approx 1$ for effective microwave heating.

A novel method has been developed and successfully demonstrated, to the best of our knowledge, for the first time to obtain the spatial electron density distribution from single-chord interferometry. To this end, the spatial power profile of the probing microwave beam, after traversing through the plasma, is measured by moving the receiving antenna of the network analyzer. This novel method allows to obtain the spatial plasma density profile by measuring only the microwave power and not the phase, removing thus the necessity of using a radiometer.

The measurements were performed above the cylindrical resonator and were compared against 3D full-wave simulations. Through this comparison the density profile was determined as centrally peaked profile. The peak density of the profile, as well as the width, are increasing with increased heating power.

Even though the applied technique of the movable receiver provides information on the density profile with a single measurement, it is only possible when there is available

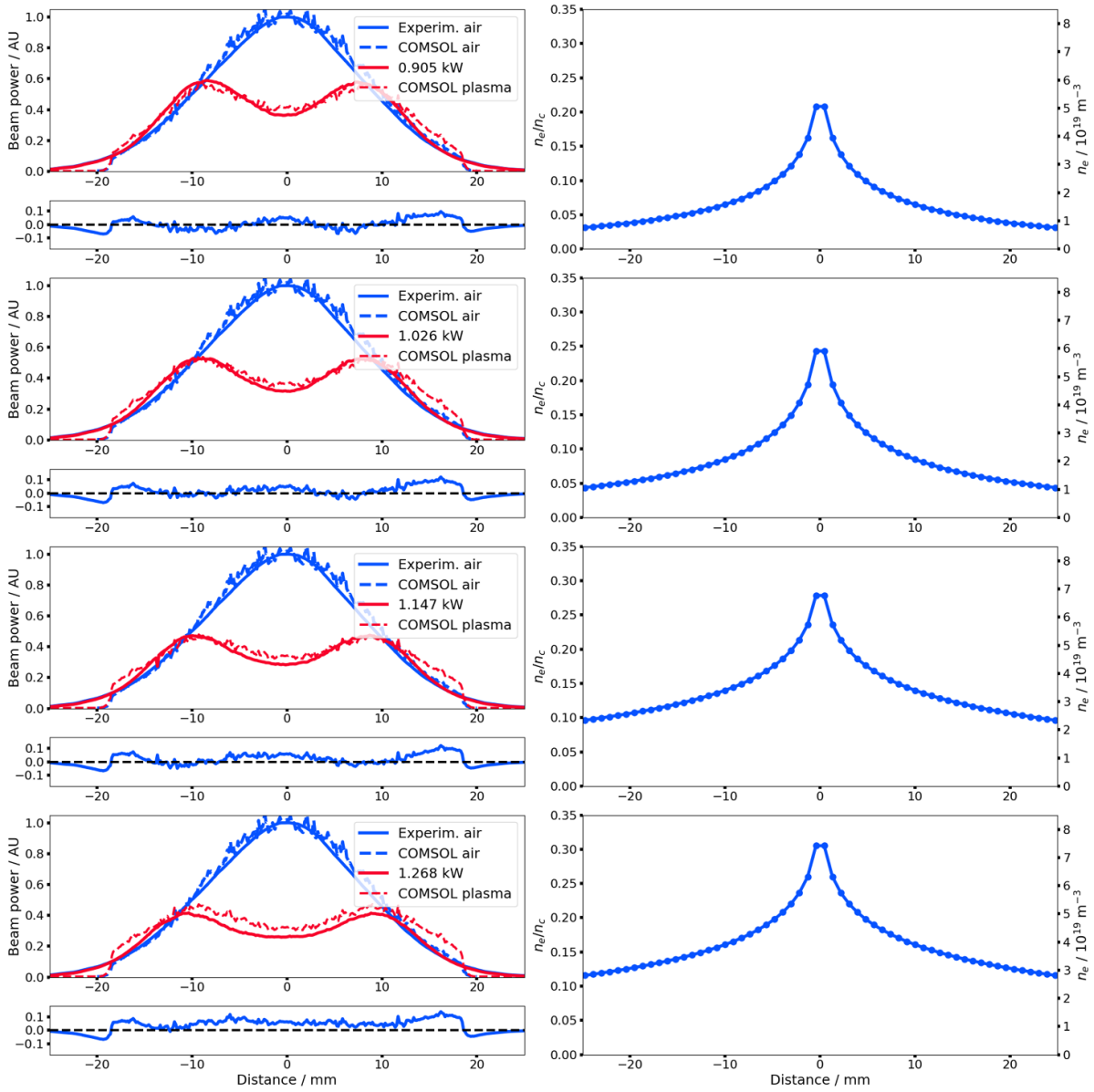


Figure 11. 3D full-wave simulation against experimental results. The beam scattering profiles are plotted on the left side for different heating powers. Below each scattering profile, the residuals are plotted as well. On the right side the plasma profile that caused the scattering profile shown on the left side is plotted.

Table 1. Parameters used in equation (10) for creating the profiles of figure 11 (right) and the R^2 score.

Input power (kW)	n_e/n_c	σ (mm)	β	R^2
0.905	0.32	2.32	0.21	0.974
1.026	0.36	2.95	0.21	0.962
1.147	0.41	5.87	0.17	0.950
1.268	0.46	5.99	0.15	0.875

space for moving a receiving antenna and steady state experimental conditions. A possible improvement of this technique would be a 1D probe array which measures the scattered power of the wave instantaneously, without the need of a moving receiver. This would allow then a real-time measurement of the electron density profile, while operating the device.

Data availability statement

The data cannot be made publicly available upon publication because they are not available in a format that is sufficiently accessible or reusable by other researchers. The data that support the findings of this study are available upon reasonable request from the authors.

Acknowledgments

The authors would like to thank Dr. Mariagrazia Troia (IGVP, University of Stuttgart) for her support in the experimental set-up of this work.

Appendix. Validation of COMSOL model

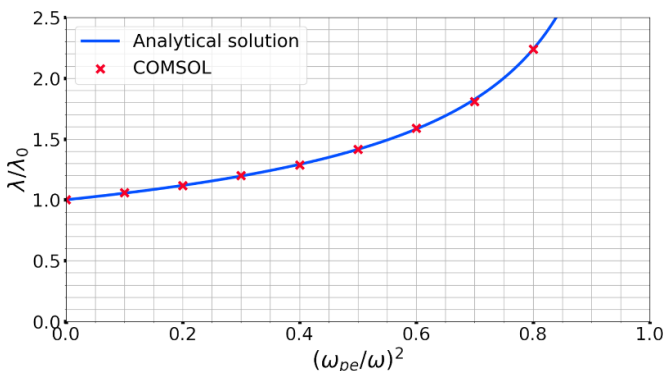


Figure 12. COMSOL benchmarking against cold plasma theory. The blue line is the analytical solution of equation (15). The COMSOL results are plotted with red crosses.

In order to ensure that the simulation is physically correct and there are no artificial effects influencing the results, a benchmarking was performed. For the purposes of the benchmarking, the plasma column was removed and the whole box was filled with plasma. The wavelength inside the plasma was calculated in COMSOL for different electron plasma densities.

Figure 12 demonstrates an excellent agreement between the 3D COMSOL model and the analytical solution of the dispersion relation for the transverse wave that propagates in an unmagnetized plasma:

$$\left(\frac{k^2 c^2}{\omega^2}\right) = 1 - \frac{\omega_{pe}^2}{\omega^2}. \quad (15)$$

ORCID iDs

Christos Vagkidis 0009-0000-8086-8843
 Andreas Schulz 0009-0009-7611-4702
 Stefan Merli 0009-0002-3335-9039
 Mirko Ramisch 0000-0002-5316-3853
 Walter Kasperek 0009-0004-5562-992X
 Günter E M Tovar 0000-0002-2437-3405
 Alf Köhn-Seemann 0000-0002-1192-2057

References

- [1] Uhm H S, Hong Y C and Shin D H 2006 A microwave plasma torch and its applications *Plasma Sources Sci. Technol.* **15** S26–S34
- [2] Ting C-C, Young T-F and Jwo C-S 2007 Fabrication of diamond nanopowder using microwave plasma torch technique *Int. J. Adv. Manuf. Technol.* **34** 316–22
- [3] Wolf A J, Peeters F J J, Groen P W C, Bongers W A and van de Sanden M C M 2020 CO_2 conversion in nonuniform discharges: disentangling dissociation and recombination mechanisms *J. Phys. Chem. C* **124** 16806–19
- [4] Wiegiers K, Schulz A, Walker M and Tovar G E M 2022 Determination of the conversion and efficiency for CO_2 in an atmospheric pressure microwave plasma torch *Chem. Ing. Tech.* **94** 299–308
- [5] Kiefer C, Antunes R, Hecimovic A, Meindl A and Fantz U 2023 CO_2 dissociation using a lab-scale microwave plasma torch: an experimental study in view of industrial application *Chem. Eng. J.* **481** 148326
- [6] Bresser M, Wiegiers K, Schulz A, Walker M and Tovar G E M 2025 Co generation from CO_2 using an atmospheric microwave plasma process *Chem. Ing. Tech.* **97** 479–86
- [7] Zheng F, Feng K, Wu S and Xiao W 2024 Experimental investigation into atmospheric microwave plasma-driven nitrogen fixation using metal–organic frameworks *Processes* **12** 2633
- [8] Troia M, Vagkidis C, Schulz A, Köhn-Seemann A, Walker M and Tovar G E M 2025 NO_x production via an atmospheric microwave air plasma torch *Chem. Ing. Tech.* **97** 435–43
- [9] Visani V J A, Patil C, Patel B K, Sharma P K, John P I and Nema S K 2014 Gliding arc triggered microwave plasma arc at atmospheric pressure for coal gasification application *Int. J. Mod. Phys.: Conf. Ser.* **32** 1460345
- [10] Hutchinson I H 2002 *Principles of Plasma Diagnostics* 2nd edn (Cambridge University Press)
- [11] Tudisco O et al 2013 A microwave interferometer for small and tenuous plasma density measurements *Rev. Sci. Instrum.* **84** 033505
- [12] Shouyin Z et al 2000 Application of far-infrared and millimeter wave techniques in plasma diagnostics in Hefei tokamaks *25th Int. Conf. on Infrared and Millimeter Waves (Cat. No.00EX442Beijing, China)* (IEEE) pp 87–88
- [13] Mott-Smith H M and Langmuir I 1926 The theory of collectors in gaseous discharges *Phys. Rev.* **28** 727–63
- [14] Douglas Swift J and Schwar M J R 1970 *Electrical Probes for Plasma Diagnostics* (Ilfie Books)
- [15] Hopwood J, Guarnieri C R, Whitehair S J and Cuomo J J 1993 Langmuir probe measurements of a radio frequency induction plasma *J. Vac. Sci. Technol. A* **11** 152–6
- [16] Fang M T C, Zhang J L and Yan J D 2005 On the use of Langmuir probes for the diagnosis of atmospheric thermal plasmas *IEEE Trans. Plasma Sci.* **33** 1431–42
- [17] Kopecki J, Kiesler D, Leins M, Schulz A, Walker M, Kaiser M, Muegge H and Stroth U 2011 Investigations of a

- high volume atmospheric plasma torch at 915MHz *Surf. Coat. Technol.* **205** S342–6
- [18] Liu Y and Hou Z 2019 Diagnostics of plasma electron density and collision frequency of fluorescent lamp using microwave transmission diagnostics *J. Phys.: Conf. Ser.* **1324** 012073
- [19] Neumann G, Bänziger U, Kammeyer M and Lange M 1993 Plasma-density measurements by microwave interferometry and Langmuir probes in an rf discharge *Rev. Sci. Instrum.* **64** 19–25
- [20] Overzet L J and Hopkins M B 1993 Comparison of electron-density measurements made using a Langmuir probe and microwave interferometer in the Gaseous Electronics Conference reference reactor *J. Appl. Phys.* **74** 4323–30
- [21] Hartfuß H-J and Geist T 2013 *Fusion Plasma Diagnostics with mm-Waves: An Introduction (Physics Textbook)* (Wiley-VCH-Verl)
- [22] Bittencourt J A and Bittencourt J A 2004 *Fundamentals of Plasma Physics* 3rd edn (Springer)
- [23] Heald M A and Wharton C B 1978 *Plasma Diagnostics With Microwaves* (R.E. Krieger Pub. Co)
- [24] Roth J R 1995 *Industrial Plasma Engineering* (Institute of Physics Publishing)
- [25] Howlader M K, Yang Y and Roth J R 2005 Time-resolved measurements of electron number density and collision frequency for a fluorescent lamp plasma using microwave diagnostics *IEEE Trans. Plasma Sci.* **33** 1093–9
- [26] Leins M, Walker M, Schulz A, Schumacher U and Stroth U 2012 Spectroscopic investigation of a microwave-generated atmospheric pressure plasma torch *Contrib. Plasma Phys.* **52** 615–28
- [27] Leins M, Kopecki J, Gaiser S, Schulz A, Walker M, Schumacher U, Stroth U and Hirth T 2014 Microwave plasmas at atmospheric pressure: microwave plasmas at atmospheric pressure *Contrib. Plasma Phys.* **54** 14–26
- [28] Leins M, Gaiser S, Schulz A, Walker M, Schumacher U and Hirth T 2015 How to ignite an atmospheric pressure microwave plasma torch without any additional igniters *J. Vis. Exp.* **98** 52816
- [29] Groen P W C, Wolf A J, Righart T W H, van de Sanden M C M, Peeters F J J and Bongers W A 2019 Numerical model for the determination of the reduced electric field in a CO₂ microwave plasma derived by the principle of impedance matching *Plasma Sources Sci. Technol.* **28** 075016
- [30] COMSOL, Inc. 2024 *RF Module User's Guide, Version 6* (COMSOL, Inc.)
- [31] Li Y and Smith. R S S 2015 Forward modeling of radio imaging (RIM) data with the Comsol RF module *Comput. Geosci.* **85** 60–67
- [32] Saini R K, Kumar A, Goyal V, Agarwal A and Prajesh R 2023 Evaluating EM-field enhancement of different shapes of metallic nanoparticles using COMSOL multiphysics for SERS-based sensors *Mater. Today: Proc.* **76** 383–7
- [33] Vencels J, Birjukovs M, Kataja J and Råback P 2019 Microwave heating of water in a rectangular waveguide: validating EOF-Library against COMSOL multiphysics and existing numerical studies *Case Stud. Therm. Eng.* **15** 100530
- [34] Xiao Y, House W, Soliman M Y, Dindoruk B and Ibragimov A 2023 Experimental, analytical and numerical study of the electromagnetic field distribution in pulsed power plasma stimulation (PPPS) *Geoenergy Sci. Eng.* **225** 211686
- [35] Zhang K, Wang S and Chen H 2023 Electromagnetic-thermal two-way coupling analysis and application on helium-cooled solid blanket *Nucl. Eng. Technol.* **55** 927–38
- [36] Wang H, Yao J, Fang C, Yuan C and Li H-P 2023 The simulation of terahertz waves transmission in the arc plasma *Front. Phys.* **11** 1182972
- [37] Leins M 2010 Development and spectroscopic investigation of a microwave plasma source for the decomposition of waste gases *PhD Thesis* Uni Stuttgart
- [38] Wolf A J, Righart T W H, Peeters F J J, Groen P W C, van de Sanden M C M and Bongers W A 2019 Characterization of CO₂ microwave plasma based on the phenomenon of skin-depth-limited contraction *Plasma Sources Sci. Technol.* **28** 115022
- [39] Marzouk. O A 2023 Temperature-dependent functions of the electron–neutral momentum transfer collision cross sections of selected combustion plasma species *Appl. Sci.* **13** 11282
- [40] Itikawa Y 2006 Cross sections for electron collisions with nitrogen molecules *J. Phys. Chem. Ref. Data* **35** 31–53
- [41] Moisan M, Ganachev I P and Nowakowska H 2022 Concept of power absorbed and lost per electron in surface-wave plasma columns and its contribution to the advanced understanding and modeling of microwave discharges *Phys. Rev. E* **106** 045202